International Journal of Solids and Structures 46 (2009) 344–363

Contents lists available at ScienceDirect

International Journal of Solids and Structures

journal homepage: www.elsevier.com/locate/ijsolstr

Characterization of mechanical properties by indentation tests and FE analysis – validation by application to a weld zone of DP590 steel

Kyung-Hwan Chung [a], Wonoh Lee [b], Ji Hoon Kim [c], Chongmin Kim [d], Sung Ho Park [a], Dongil Kwon [e], Kwansoo Chung [e,*]

[a] Automotive Steel Applications Research Group, Technical Research Labs, POSCO, 699 Gumho-dong, Gwangyang, Jeonnam 545-090, Republic of Korea
[b] Composite Materials Research Group, Korea Institute of Materials Science, 531 Changwon-daero, Changwon, Kyungnam 641-010, Republic of Korea
[c] Department of Materials Science and Engineering, Ohio State University, 2041 College Road, Columbus, OH 43210, USA
[d] Materials and Process Lab., R&D Center & NAO Planning General Motors, Warren, MI 48090-9055, USA
[e] Department of Materials Science and Engineering, Intelligent Textile System Research Center, Seoul National University, 56-1, Shinlim-dong, Kwanak-ku, Seoul 151-742, Republic of Korea

ARTICLE INFO

Article history:
Received 22 June 2008
Received in revised form 22 August 2008
Available online 12 September 2008

Keywords:
DP-steel
MAG weld zone
Strain-rate sensitivity
Formability
Continuous indentation method

ABSTRACT

In this work, the mechanical properties of the metal active gas (MAG) weld zone and heat affected zone (HAZ) were characterized utilizing the continuous indentation method together with its finite element (FEM) analysis. To verify the measured properties, uni-axial tension and three point bending tests were performed for DP590 welded specimens. For numerical simulations, the isotropic hardening law was assumed along with the non-quadratic anisotropic yield function, Yld2000-2d. As for the failure criterion of the base material and weld zones particularly for the failure evaluation in the uni-axial tension test, Hill's bifurcation theory and the *M–K* theory were applied to calculate the forming limit diagrams considering all measured properties including strain-rate sensitivity.

1. Introduction

The welding process plays an important role in the automotive industry since all parts are ultimately assembled together through welding and joining. Therefore, many welding technologies were developed for various purposes such as metal active gas (MAG), tungsten inert gas (TIG), electrical resistance spot (ERS) welding and so on (Gery et al., 2005; Aslanlar et al., 2007; Liu et al., 2007). Recently, in order to save materials and reduce the weight of vehicles, automotive companies put forth efforts to form body panels by utilizing tailor-welded blanks (TWB) made of various advanced materials (Saunders and Wagoner, 1996). Laser welding and friction stir welding (FSW) processes have been popular in manufacturing steel and aluminum alloy TWB, respectively (Sato et al., 2004; Qiu and Chen, 2007).

As for the performance evaluation of welded automotive components with respect to durability or crashworthiness, it is important to properly account for the property change (near and) in the weld zone, since the base material undergoes significant mechanical property changes when welded as a result of welding heat effects. In particular, the slow cooling condition after welding processes can induce the heat affected zone (HAZ) to soften for high-strength steels (Thaulow et al., 1994; Wojnowski et al., 2000). In order to predict the overall mechanical behavior of the welded high-strength steel sample, the effects of the assumed amount of softness and the size of the HAZ area were successfully evaluated on crack behavior (Rodrigues et al., 2004a) and tensile performance (Rodrigues et al., 2004b), confirming the necessity of characterized mechanical properties of the HAZ as

* Corresponding author. Tel.: +82 2 880 7189; fax: +82 2 885 1748.
E-mail address: kchung@snu.ac.kr (K. Chung).

0020-7683/$ - see front matter © 2008 Elsevier Ltd. All rights reserved.
doi:10.1016/j.ijsolstr.2008.08.041

well as the weld zone for reliable performance predictions in the process design stage. Recently, methods to characterize the weld zone properties of the laser welded or friction stir welded TWB sheets have been developed based on the uni-axial tension test in conjunction with the rule of mixture (Abdullah et al., 2001) or the uni-axial tension test with ASTM sub-sized specimens (Woo et al., 2006). However, the size of the area represented by the average measured properties is rather coarse for the method of the rule of mixture, while preparing very small sub-sized specimens is a rather difficult task for MAG, TIG and ERS welding processes. Therefore, the continuous indentation method was applied in this work, together with its finite element (FEM) analysis, to characterize the mechanical properties of the metal active gas (MAG) weld zone and HAZ.

Not requiring sophisticated instruments, the indentation test has been widely applied to determine mechanical properties of various materials, often as a substitute to the standard tension test, especially when the standard test is difficult to apply. In the early stage, hardness (average contact pressure) and yield strength were mainly evaluated from the measurement of the residual imprint size (Tabor, 1951). The ratio between hardness and flow stress was also investigated as a function of the sharp indenter angle to estimate the constitutive behavior (Dugdale, 1954). Later, tensile strength at various strains was obtained utilizing miscellaneous indenters with different shapes (ball or pyramid) and sizes (Millman et al., 1993; Chollacoop and Ramamurty, 2005).

After the depth-sensing instrumented indentation was developed, in which the indenting load can be continuously monitored as a function of the penetration depth during loading/unloading procedures, much research has been done to extract mechanical properties from indentation responses. Young's modulus and hardness were obtained from the maximum load and the initial unloading slope using sharp indenters (Doerner and Nix, 1986; Oliver and Pharr, 1992). Also, Young's modulus and Poisson's ratio were assessed analytically and computationally for a graded elastic substrate (Giannakopoulos and Suresh, 1997a,b; Suresh et al., 1997). Recently, the elasto-plastic properties including yield stress and the strain-hardening exponent were determined by analyzing the measured load–depth curves with sharp indenters such as Vickers and Berkovich (Giannakopoulos and Suresh, 1999; Venkatesh et al., 2000; Dao et al., 2001; Chollacoop et al., 2003; Casals and Alcalá, 2005; Antunes et al., 2007) or spherical indenters (Tirupataiah and Sundararajan, 1991; Zeng et al., 1996; Alcalá et al., 1998; Ahn and Kwon, 2001; Jang et al., 2005a). However, these methods were mainly developed for particular hardening laws (such as the Hollomon type law) so that the reverse method based on finite element simulations was developed here, which can be applicable for various hardening laws. Particularly, the Swift hardening law was applied in this work. As for the indenter, the spherical one was used here to perform axi-symmetric simulations with an aim to effectively reduce computational efforts.

In recent years, automotive companies put forth major efforts to reduce the weight of vehicles in response to environmental issues such as air pollution and high energy prices. For this reason, the demand for light-weight and/or high-strength sheet metals such as aluminum alloys and advanced high-strength steels (AHSS) has increased in automotive applications. Among these new automotive materials, dual phase steel (DP-steel) is particularly suitable for structural components such as engine cradles because of its superior combination of ductility and strength (Paruz and Edmonds, 1989). Also, DP-steel demonstrates no yield point elongation unlike the traditional high-strength low-alloy (HSLA) steel (Chen et al., 2001). Furthermore, compared to HSLA steel, DP-steel has a higher strain-hardening rate, which enhances more uniform deformation in the forming process and contributes to the absorption of more impact energy (Fekete et al., 2001). Based on these reasons, the mechanical properties of MAG weld zones and HAZ were measured for DP590 sheets with 2.0 mm thickness for this work in an effort to improve the accuracy of evaluating the performance of DP-steel automotive parts. Compared to conventional automotive steels, weldability of the DP-steel is nearly comparable (Marya and Gayden, 2005), though slightly worse than the mild steel, while Al/Mg alloys have worse weldability (Jang et al., 2005b; Afrin et al., 2008).

To verify the measured weld zone properties, uni-axial tension and three point bending tests were performed for welded specimens. For numerical simulations, the isotropic hardening law was assumed along with the non-quadratic anisotropic yield function, Yld2000-2d (Barlat et al., 2003), which is valid for the plane stress condition, while isotropy was assumed for the weld zones. Note that one of the main objectives of the numerical method developed in this work is to ultimately apply this method to the forming analysis and the performance evaluation of formed automotive parts made of various advanced automotive sheets in the future. Therefore, material properties were measured rather rigorously utilizing the recently developed yield function. Also, since computational efficiency is so critical in extended future work, the 2D numerical model under the plane stress condition was imposed in this work due to its computational efficiency compared to the full 3D condition.

The constitutive laws were implemented into ABAQUS/Standard code utilizing the user subroutine. As for the failure criterion of the base material and weld zones, particularly for the failure evaluation in the uni-axial tension test, Hill's bifurcation theory and the *M–K* theory (Marciniak and Kuczynski, 1967) were applied to calculate the forming limit diagrams considering all measured properties including strain-rate sensitivity. In Section 2, the anisotropic yield stress potential Yld2000-2d as well as the numerical formulation is briefly reviewed. In Section 3, the mechanical properties of the base material and the weld zones are characterized. In Section 4, the measured properties of the weld zones are verified with uni-axial tension and three point bending tests.

2. Theory

2.1. Plane stress yield function: Yld2000-2d

In order to describe the initial anisotropic yield stress surface, the yield stress function Yld2000-2d proposed by Barlat et al. (2003) was considered. Compared to the yield stress functions previously proposed by Barlat et al. (1989, 1991,

1997), this yield function has enough anisotropic coefficients to accommodate eight mechanical measurements and the convexity of the yield surfaces is also well proven. These eight mechanical measurements to represent orthogonal anisotropy are typically σ_0, σ_{45}, σ_{90}, R_0, R_{45}, R_{90}, σ_b and R_b, which are simple tension yield stresses along the rolling (x-) direction, 45° off and transverse (y-) directions, R-values (width-to-thickness strain ratio in simple tension), yield stress and in-plane principal strain ratio under the balanced biaxial tension condition, respectively.

The yield stress function for the plane stress condition, Yld2000-2d, is defined by two linear transformation tensors; i.e.

$$f^{\frac{1}{M}} = \left\{\frac{\Phi}{2}\right\}^{\frac{1}{M}} = \bar{\sigma} \tag{1}$$

where $\bar{\sigma}$ is the effective stress and M is the yield exponent. Also, in Eq. (1)

$$\Phi = |\widetilde{S}'_{\mathrm{I}} - \widetilde{S}'_{\mathrm{II}}|^M + |2\widetilde{S}''_{\mathrm{II}} + \widetilde{S}''_{\mathrm{I}}|^M + |2\widetilde{S}''_{\mathrm{I}} + \widetilde{S}''_{\mathrm{II}}|^M \tag{2}$$

In Eq. (2), $\widetilde{S}'_k$ and $\widetilde{S}''_k (k = \mathrm{I}, \mathrm{II})$ are the principal values of the symmetric tensor $\tilde{\mathbf{s}}(\tilde{\mathbf{s}}'$ or $\tilde{\mathbf{s}}'')$, in which

$$\begin{aligned} \tilde{\mathbf{s}}' &= \mathbf{C}' \cdot \mathbf{s}, \\ \tilde{\mathbf{s}}'' &= \mathbf{C}'' \cdot \mathbf{s} \end{aligned} \tag{3}$$

Here, $\mathbf{C}'$ and $\mathbf{C}''$ contain anisotropic coefficients and $\mathbf{s}$ is the deviator of the Cauchy stress tensor. The two associated linear transformations are

$$\mathbf{C}' = \begin{bmatrix} c'_{11} & c'_{12} & 0 \\ c'_{21} & c'_{22} & 0 \\ 0 & 0 & c'_{66} \end{bmatrix} \tag{4}$$

and

$$\mathbf{C}'' = \begin{bmatrix} c''_{11} & c''_{12} & 0 \\ c''_{21} & c''_{22} & 0 \\ 0 & 0 & c''_{66} \end{bmatrix} \tag{5}$$

Note that there are ten anisotropic coefficients in Eqs. (4) and (5), but only three are independent in Eq. (4) (so that only eight are independent as a whole). This is because c'_{12} and c'_{21} are dependently related to c'_{11} and c'_{22}, respectively, in order to have the unique $|\widetilde{S}'_{\mathrm{I}} - \widetilde{S}'_{\mathrm{II}}|$ in Eq. (2). To have eight independent coefficients, one choice is to set $c'_{12} = c'_{21} = 0$.

2.2. Numerical formulation for stress integration

In this paper, the additive decoupling of the total strain increment into the elastic and plastic strain increments, $d\boldsymbol{\varepsilon} = d\boldsymbol{\varepsilon}^{\mathrm{p}} + d\boldsymbol{\varepsilon}^{\mathrm{e}}$, and the associated flow rule based on the normality rule are assumed. For the numerical formulation for large deformation, the incremental deformation theory based on the minimum plastic work deformation (Chung and Richmond, 1993) was applied to the elasto-plastic formulation. Under this scheme, the strain increment in the flow formulation becomes the discrete true strain increment while a material rotates by incremental rotation obtained from the polar decomposition at each discrete step.

In the stress update scheme, the updated stress is initially assumed to be elastic for a given discrete strain increment $\Delta\boldsymbol{\varepsilon}$. Therefore

$$\boldsymbol{\sigma}^{\mathrm{T}}_{n+1} = \boldsymbol{\sigma}_n + \mathbf{C} \cdot \Delta\boldsymbol{\varepsilon} \tag{6}$$

where the superscript T stands for a trial state and the subscript denotes the process time step, and $\mathbf{C}$ is the elastic modulus. Also, preserving the plastic quantities as the previous values

$$\bar{\varepsilon}^{\mathrm{T}}_{n+1} = \bar{\varepsilon}_n, \quad \dot{\bar{\varepsilon}}^{\mathrm{T}}_{n+1} = \dot{\bar{\varepsilon}}_n \tag{7}$$

where $\bar{\varepsilon} (\equiv \int \mathrm{d}\bar{\varepsilon})$ is the accumulative effective strain. If the following yield condition is satisfied with trial values for an elastic tolerance $\mathrm{Tol}^{\mathrm{e}}$, which is prescribed as 10^{-5} in this work; i.e.

$$f^{\frac{1}{M}}(\boldsymbol{\sigma}^{\mathrm{T}}_{n+1}) - \bar{\sigma}(\bar{\varepsilon}^{\mathrm{T}}_{n+1}, \dot{\bar{\varepsilon}}^{\mathrm{T}}_{n+1}) < \mathrm{Tol}^{\mathrm{e}} \tag{8}$$

then, the process time step $n+1$ is considered elastic. However, if the above yield condition is violated, the step is considered elasto-plastic and the trial elastic stress state is taken as an initial value for the solution of the plastic corrector problem. The non-linear equation to solve for $\Delta\bar{\varepsilon}$, which enables resulting stresses to stay on the hardening curves at the new step $n+1$, is

$$f^{\frac{1}{M}}(\boldsymbol{\sigma}_n + \Delta\boldsymbol{\sigma}) = \bar{\sigma}\left(\bar{\varepsilon}_n + \Delta\bar{\varepsilon}, \frac{\Delta\bar{\varepsilon}}{\Delta t}\right) \tag{9}$$

The elastic predictor–plastic corrector scheme based on the Newton–Raphson method was used to solve Eq. (9) (Chung et al., 2005). After obtaining the converged solution of Eq. (9), the stresses and equivalent plastic strain are updated for the next step. Based on the numerical formulation discussed here, the constitutive law for the isotropic hardening behavior was implemented into the ABAQUS/Standard commercial code using the user-defined materials subroutine.

3. Material properties

Uni-axial tension tests were performed for the DP590 base sheet (with 2 mm thickness) to measure hardening, yield strength and *R*-values along 0°, 45°, 90° off the rolling direction. The strain-rate sensitivity was also measured using the high speed tension tests. The mechanical properties of the weld zones were also obtained conjointly utilizing the continuous indentation method and its FEM analysis. The forming limit diagram for the base material was measured experimentally, while those for weld zones were calculated based on Hill's bifurcation theory and the *M–K* theory (Marciniak and Kuczynski, 1967).

3.1. DP590 base sheet

The DP590 base sheet was characterized utilizing uni-axial tension tests in order to calculate the coefficients of the 2D yield stress function under the plane stress condition, Yld2000-2d. The rolling, 45°, and transverse tests in uni-axial tension were conducted utilizing the ASTM E 8M subsize and ASTM E 517 standard specimens. The dimensions (gauge length × width) of those specimens are 25 mm × 6 mm and 50 mm × 12.5 mm, respectively. Note that the ASTM E 517 specimen was used only for plastic strain ratio (*R*-value) measurements. Tension tests were performed with Zwick's 10-t tension test machine (model: Z-100) with constant cross-head speeds 0.05 and 0.1 mm/s for the ASTM E 8M subsize and ASTM E 517 standard specimens, respectively. For standard specimens, extension data were collected with the extensometer (Zwick's Macro-Standard Extensometer made in F. R Germany; gauge length: 12.5 mm). Hydraulic grips were used to simultaneously clutch the two ends of the specimen. The measured results of the hardening behaviors for the rolling, 45°, and transverse directions are shown in Fig. 1. The measured Young's modulus, the average 0.2% offset yield strength (YS), ultimate tensile strength (UTS) and *R*-values that were determined from the directional tests are summarized in Table 1. The measured Young's modulus corresponds well with values obtained from other sources (Nakamachi et al., 2001). Poisson's ratios of DP590 base sheet were obtained from literatures (Nakamachi et al., 2001).

The six measured material data (three uni-axial yield stresses and three *R*-values in the three material directions) and one assumed data on the balanced biaxial yield stress ($\sigma_b = \sigma_0$) were utilized in order to calculate the anisotropic coefficients of Yld2000-2d, after assuming $L''_{12} = L''_{21}$ as suggested by Barlat et al. (2003). Note that the assumed σ_b (=σ_0) is based on the previous experimental result obtained for DP-steel having similar strength (Lee et al., 2005), while the assumption $L''_{12} = L''_{21}$ is to eliminate one coefficient, especially when R_b is not available. The calculation procedure involves solving a system of non-linear equations, in which seven coefficients were obtained using the regular Newton–Raphson iteration method. Input data for the calculation of the anisotropic coefficients of Yld2000-2d are summarized in Table 2. The exponent of yield stress functions accounts for the crystal structure so that the value recommended in crystal plasticity was used in this paper (Hosford, 1972; Logan and Hosford, 1980): for DP-steel, $M = 6.0$ as BCC. The resulting anisotropic coefficients of Yld2000-2d obtained are summarized in Table 3. The yield stress surface, the normalized stresses and *R*-values calculated from Yld2000-2d for the DP590 base sheet are shown in Fig. 2.

The true stress-true plastic strain data measured in the directional uni-axial tension tests conducted for each direction were fit to the Swift equation as Eq. (10):

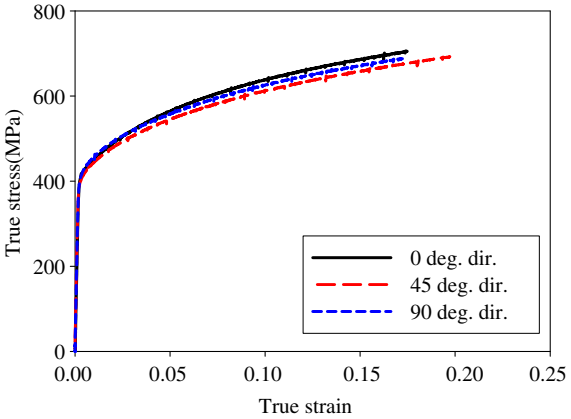

Fig. 1. Hardening behaviors of the DP590 base sheet for the rolling, 45°, and transverse directions.

Table 1
Plastic properties of the DP590 base sheet

Material	Direction (°)	Young's modulus (GPa)		Poisson's ratio	YS (MPa)	UTS (MPa)	*R*-Value
		Measured	Referred				
DP590 base sheet	0	214.2 ± 0.726	210*	0.3[a]	418.3	591.5	0.776
	45				409.3	568.4	1.050
	90				420.0	578.6	1.030

[a] Referred by the reference (Nakamachi et al., 2001).

Table 2
The normalized yield stresses in the three material directions and the balanced biaxial yield stress (normalized by the rolling direction uni-axial yield stress) with *R*-values in the uni-axial tension test for the DP590 base sheet

Material	χ_0	χ_{45}	χ_{90}	χ_b	R_0	R_{45}	R_{90}
DP590 base sheet	1.000	0.978	1.004	1.000[a]	0.776	1.050	1.030

[a] Assumed.

Table 3
Anisotropic coefficients of Yld2000-2d for the DP590 base sheet

M	c'_{11}	c'_{22}	c'_{66}	c''_{11}	c''_{12}	c''_{21}	c''_{22}	c''_{66}
6.0	0.931	1.042	1.023	1.028	0.003	−0.018	0.986	1.043

$$\bar{\sigma} = K(\bar{\varepsilon}_0 + \bar{\varepsilon}^p)^n \left(\frac{\dot{\bar{\varepsilon}}^p}{\dot{\bar{\varepsilon}}_0}\right)^m \tag{10}$$

For each case, three to five tests were performed and one optimized curve within the average range was chosen to calculate the constants. The Swift constants obtained with the reference strain-rate $\dot{\bar{\varepsilon}}_0 = 1.25 \times 10^{-3}$ s^{-1} (with the cross-head speed 0.05 mm/s) are listed in Table 4. As for the hardening behavior, the uni-axial tension data along the rolling direction were considered as the reference state for the isotropic hardening law.

Strain-rate sensitivity tests were carried out at the room temperature utilizing the modified specimen whose gauge length is 32 mm as shown in Fig. 3. Dynamic uni-axial tension tests (Huh et al., 2004) were performed with four constant cross-head speeds: 0.032, 0.32, 3.2 and 6.4 m/s. These cross-head speeds give the true strain-rates 0.9, 9.0, 90.0 and 180.0 s^{-1}, respectively. The measured engineering stress–strain curves were plotted in Fig. 4, which shows that the flow stress increases with the strain-rate. The strain-rate sensitivity is often described by the power law relationship such as Eq. (10). In order to obtain the strain-rate sensitivity index, *m*, two continuous stress–strain curves at different strain-rates are compared at the same strain using the equation

$$m = \frac{\ln(\sigma_2/\sigma_1)}{\ln(\dot{\varepsilon}_2/\dot{\varepsilon}_1)} \tag{11}$$

Here, σ_1 and σ_2 represent the (true) flow stresses at two true strain-rates $\dot{\varepsilon}_1$ and $\dot{\varepsilon}_2$, respectively. Strain-rate sensitivity indices were computed for strain-rate ratios 1:10, 1:100 and 1:200 with 0.9 s^{-1} as the base strain-rate with respect to the true strain within the plastic deformation range. Then, the average strain-rate sensitivity index, m = 0.0145, was obtained for the DP590 base sheet.

Forming limit diagram for the DP590 base sheet was measured experimentally as shown in Fig. 5. In order to enhance the reliability of calculated FLDs for weld zones, FLD calculation utilizing Hill's bifurcation theory (for the left side of the diagram) and the *M–K* theory (for the right hand side of the diagram) along with the implemented Yld2000-2d was also conducted. For the calculation of the *M–K* theory, the initial defect parameter D_0, which is 0.9997, was obtained such that the FLD_0 values (the forming limit values under the plane strain condition) calculated from Hill's bifurcation and the *M–K* theories coincide (in the middle of the diagrams). Since Hill's bifurcation theory can not account for strain-rate sensitivity, the initial defect parameter was obtained without considering strain-rate sensitivity. Then, the obtained defect size was used to calculate the forming limit diagrams considering the strain-rate sensitivity. The calculated results are shown in Fig. 5, which confirm that the forming limits with strain-rate sensitivity are higher than those without strain-rate sensitivity.

The calculated FLD of the DP590 base sheet was compared with the experimental data obtained under the static condition in Fig. 5. The predicted FLD curve showed reasonably good agreement with the measurement, especially for the plane strain mode and the left side of the diagram. This result suggests that the FLD calculated based on Hill's bifurcation and *M–K* theories is useful since failure at the plane strain mode is most dominant for forming applications. Also note that the relative difference of the calculated FLD is useful enough for overall formability performance evaluation so that the absolute FLD evaluation at each weld material is not intended.

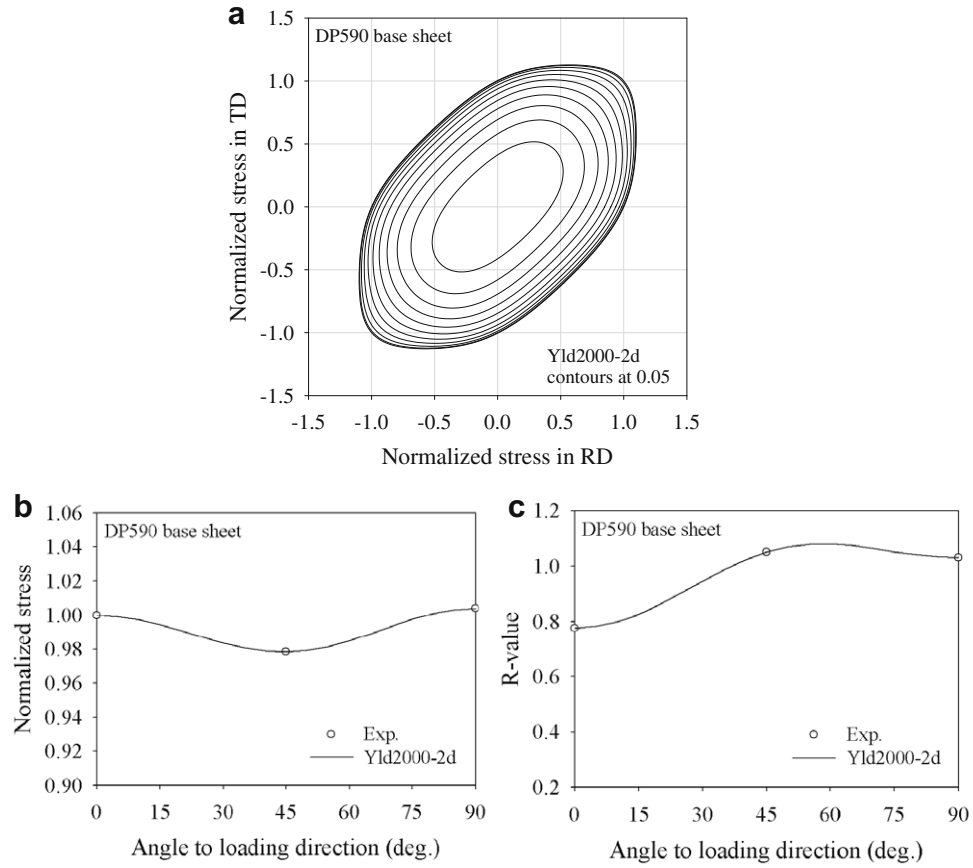

Fig. 2. Characteristics of Yld2000-2d for the DP590 base sheet: (a) yield surface contour and the anisotropies of (b) normalized stress and (c) *R*-value.

Table 4
Hardening descriptions of the DP590 base sheet for uni-axial tension tests

Material	Direction (°)	Swift		
		n	K (MPa)	$\bar{\varepsilon}_0$
DP590 base sheet	0	0.231	1042.3	0.0224
	45	0.238	999.1	0.0295
	90	0.227	1005.2	0.0266

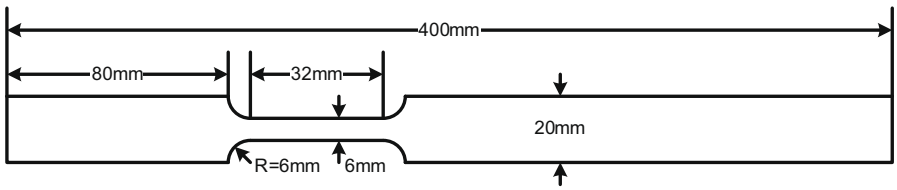

Fig. 3. The specified tension specimen for the strain-rate sensitivity test of the DP590 base sheet.

3.2. Metal active gas (MAG) weld zone and heat affected zone (HAZ)

In order to characterize the mechanical properties of the MAG weld zone and HAZ, the continuous indentation method and its FEM analysis were performed. Fig. 6(a) shows the schematic view of the welded DP590 sheet specimen for the indentation test. It can be seen in this figure that, after the upper DP590 sheet plate was placed on the top of the lower plate aligned with the rolling direction, the upper and lower plates were welded together along the direction of the boundary line (aligned along the rolling direction).

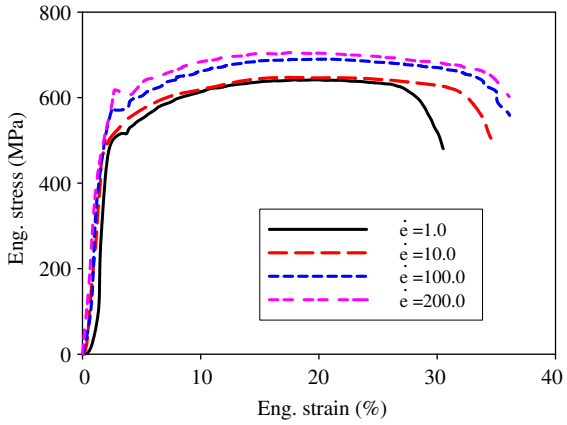

Fig. 4. Engineering stress–strain curves of the DP590 base sheet for various strain-rate levels.

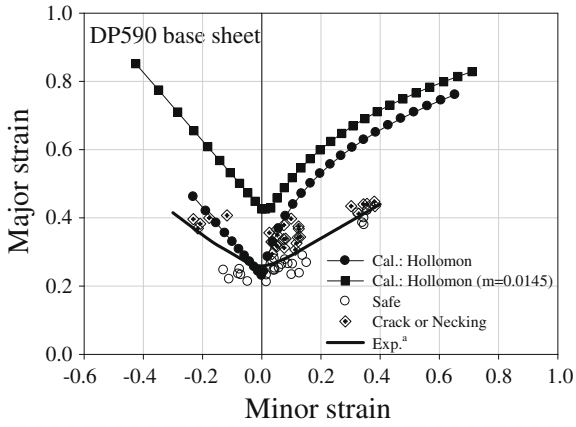

Fig. 5. Experimental and calculated forming limit diagrams for the DP590 base sheet.

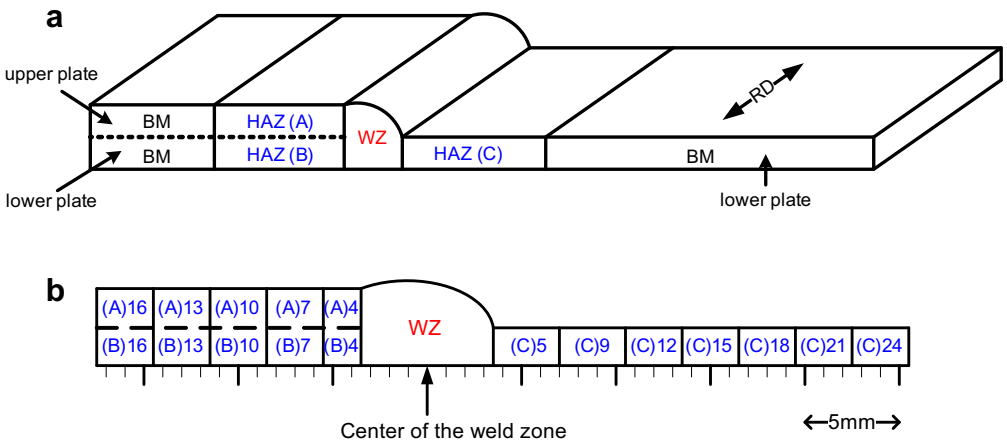

Fig. 6. The welded DP590 sheet specimen for the continuous indentation test: (a) schematic view (b) enlarged cross-section view near the weld zone.

As illustrated in Fig. 7, the measured load–depth curves for the DP590 base sheet material and the weld zones at various locations away from the center of the weld zone were obtained utilizing the AIS2100 indentation machine whose indenter is the sphere with 0.5 mm diameter. The indentation tests were performed discretely at each location, assuming stepwise

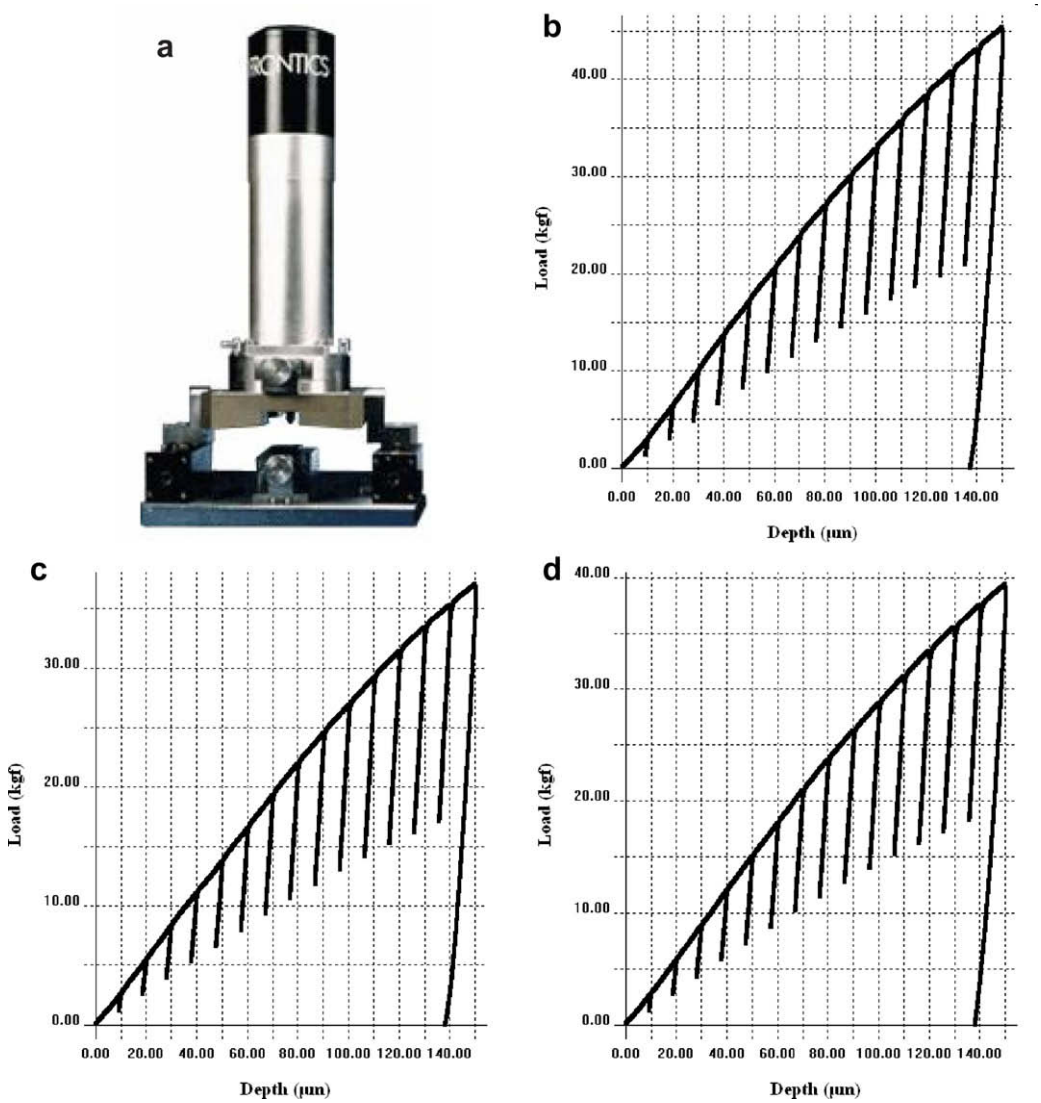

Fig. 7. Continuous indentation test: (a) AIS2100 indentation test machine and experimental load–depth curves for (b) weld zone, (c) HAZ(C)-5 and (d) base material.

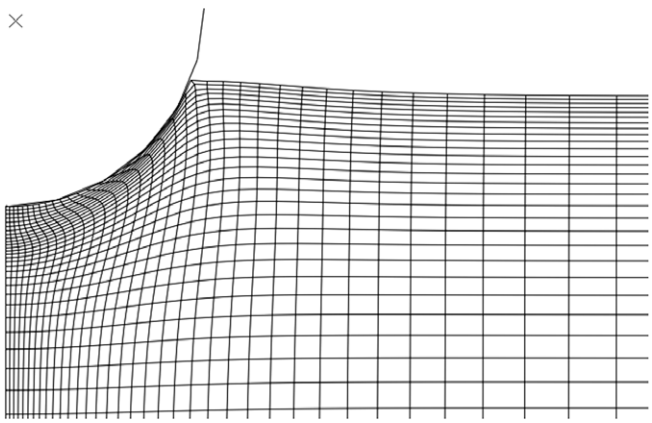

Fig. 8. Finite element simulation for the continuous indentation test.

Table 5
Hardening parameters of the weld zone and HAZ

Material	Position[a] (mm)	Swift		
		n	K (MPa)	$\bar{\varepsilon}_0$
MAG weld zone	0	0.18	1140	0.013
HAZ(A)	4	0.16	840	0.012
	7	0.17	940	0.010
	10	0.16	980	0.013
	13	0.16	980	0.009
	16	0.16	960	0.010
HAZ(B)	4	0.20	900	0.003
	7	0.19	1000	0.011
	10	0.17	1000	0.013
	13	0.18	960	0.010
	16	0.19	980	0.009
HAZ(C)	5	0.16	820	0.009
	9	0.16	960	0.011
	12	0.14	960	0.010
	15	0.15	960	0.013
	18	0.15	950	0.010
	21	0.15	900	0.013
	24	0.20	980	0.013

[a] Positions away from the center of the MAG weld zone.

homogeneous properties of the weld zones with 7.0 mm (for MAG weld zone) and 2.0–3.5 mm (for HAZ) widths as shown in Fig. 6(b). Note that, in consideration of the asymmetry of the HAZ, the load–depth curves for the A–C regions of the HAZ at various locations away from the weld zone (see Fig. 6) were measured respectively.

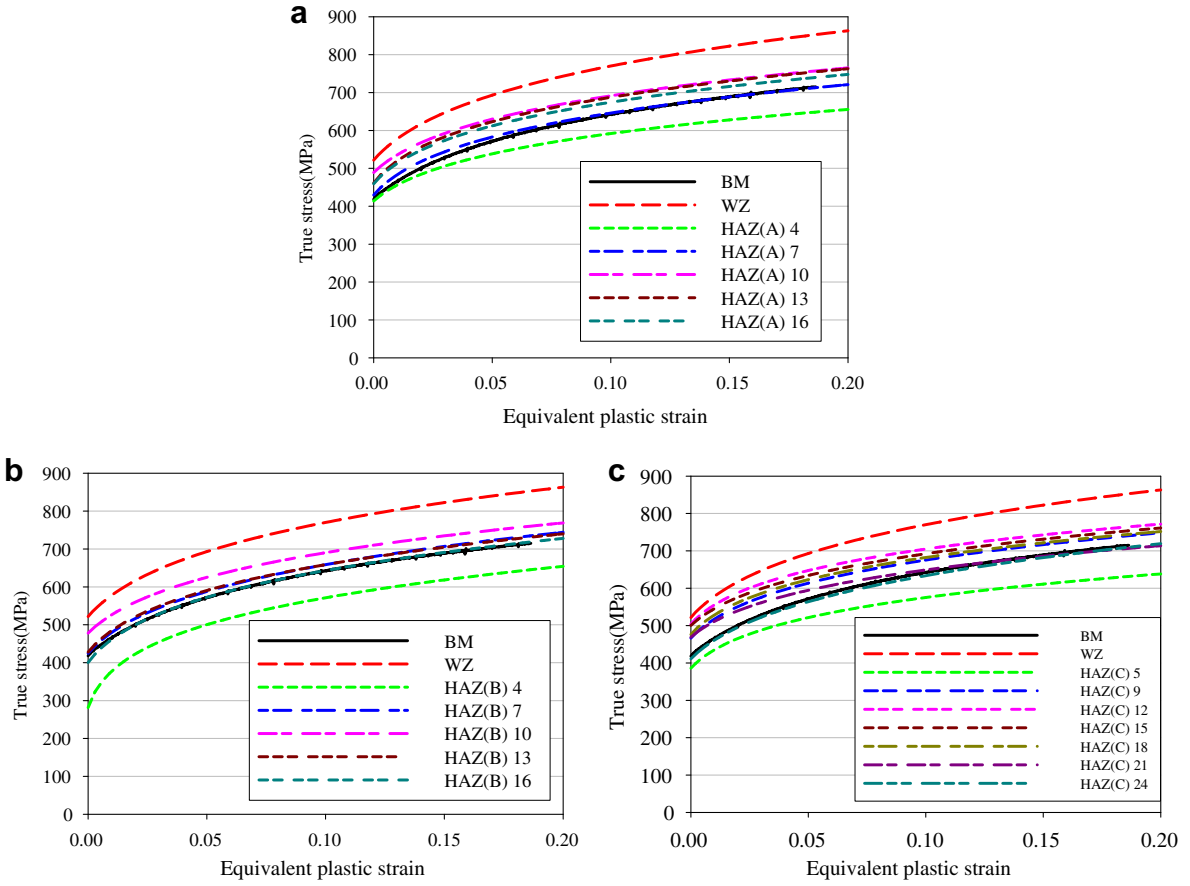

Fig. 9. The hardening curves for the weld zone and HAZ: (a) HAZ(A), (b) HAZ(B) and (c) HAZ(C) (the number # in HAZ # represents the distance from the weld zone center).

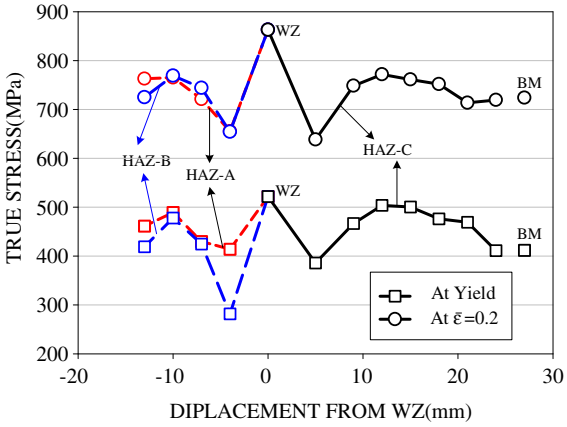

Fig. 10. The yield stress distributions for all locations of the welded DP590 sheet.

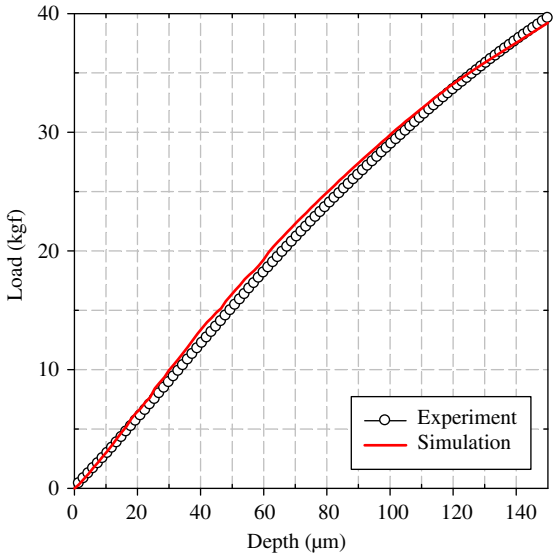

Fig. 11. Comparison of the calculated and measured load–depth curves of the indentation test performed for the base material.

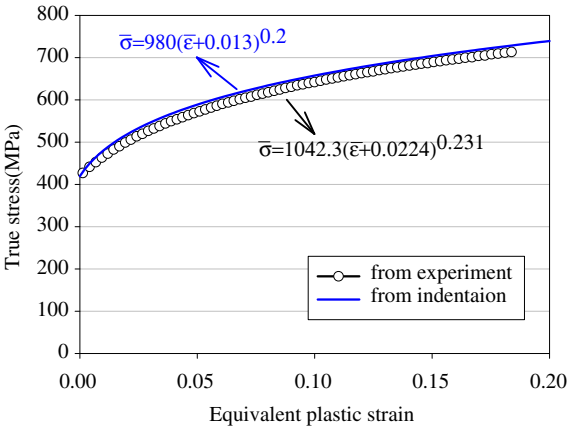

Fig. 12. The hardening curves determined from the reverse method and measured from the uni-axial tension test for the base material.

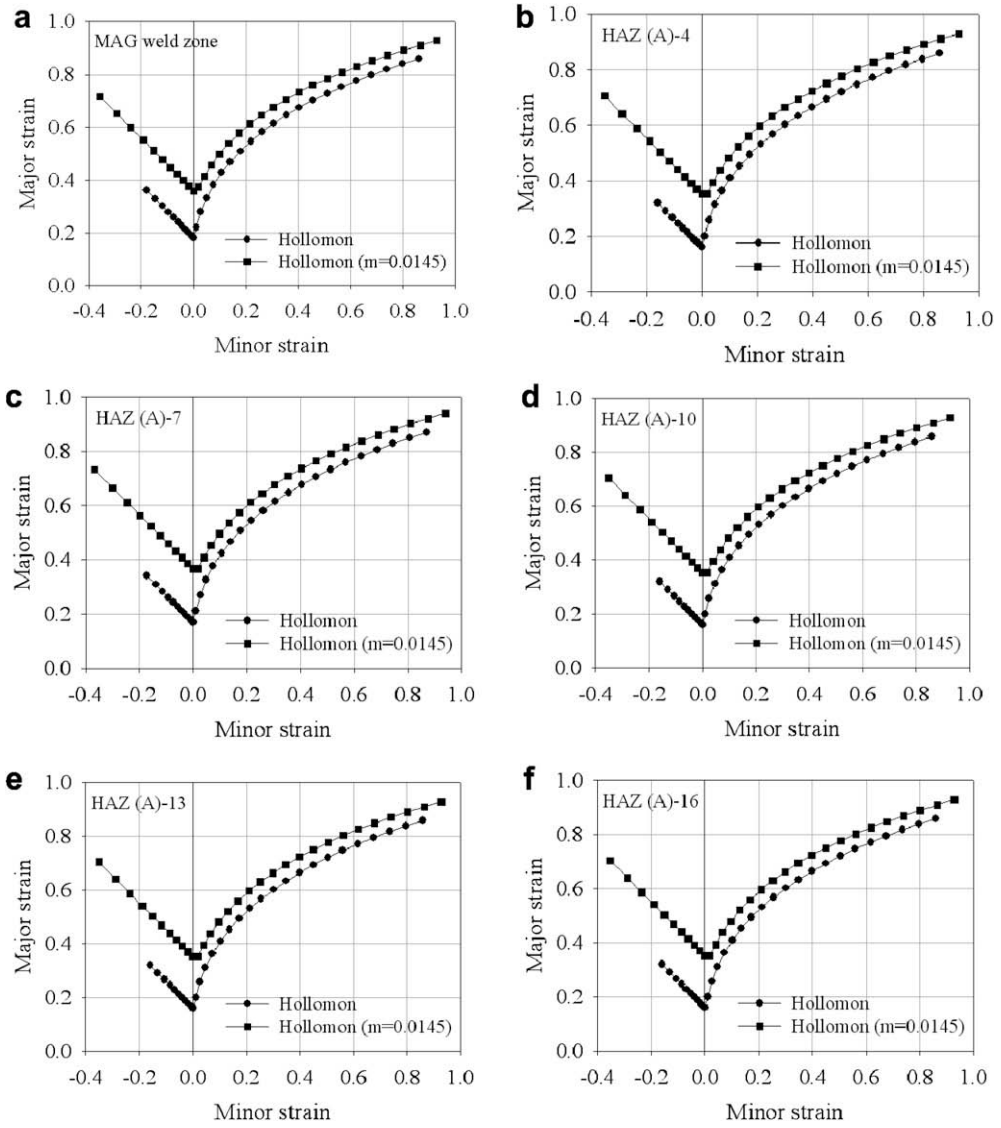

Fig. 13. Calculated forming limit diagrams for (a) weld zone and HAZ(A): (b) HAZ(A)-4, (c) HAZ(A)-7, (d) HAZ(A)-10, (e) HAZ(A)-13 and (f) HAZ(A)-16 (the number # in HAZ # represents the distance from the weld zone center).

As shown in Fig. 8, (axi-symmetric) finite element analysis for the indentation test was performed in order to determine the hardening parameters for the weld zones (including HAZ) by comparing the measured load–depth curves with a set of calculated load–depth curves prepared in advance. For the simulations, the isotropic hardening law based on the Swift equation shown in Eq. (10) was applied, while the strain-rate sensitivity of the base material was assumed for the weld zones. Also, since the yield function Yld2000-2d cannot account for the axi-symmetric analysis and is valid only for the plane stress condition, the Mises yield function was utilized assuming isotropy in the weld zones for simplicity. The ABAQUS/Standard code with total 2500 four-node axi-symmetric solid (CAX4) elements was used, while the friction coefficient was assumed 0.11. This friction coefficient was numerically obtained so that, with this particular value, the simulated load–depth curve based on the hardening curve in the rolling direction of the base material was compatible with the measured curve (here, the moderate amount of anisotropy of the base material partially justify the use of the Mises criterion).

As for the set of the prepared curves, indentation simulations were carried out for the total of 840 different combinations of the hardening parameters, in which K varied from 800 to 1200 MPa (for every 20 MPa); n varied from 0.14 to 0.21 (for every 0.01); ε_0 varied from 0.009 to 0.013 (for every 0.001). The load–depth curves, calculated up to 0.15 mm penetration depth, were compared with the measured ones to determine the hardening parameters. Note that only the load–depth curves were used to evaluate hardening curves, not the elastic unloading and loading curves. The hardening parameters which gave the best agreements between the calculated and measured load–depth curves are listed in Table 5 and the resulting hardening curves are plotted in Fig. 9. The number # in HAZ # in the figure represents the distance (in mm) from the

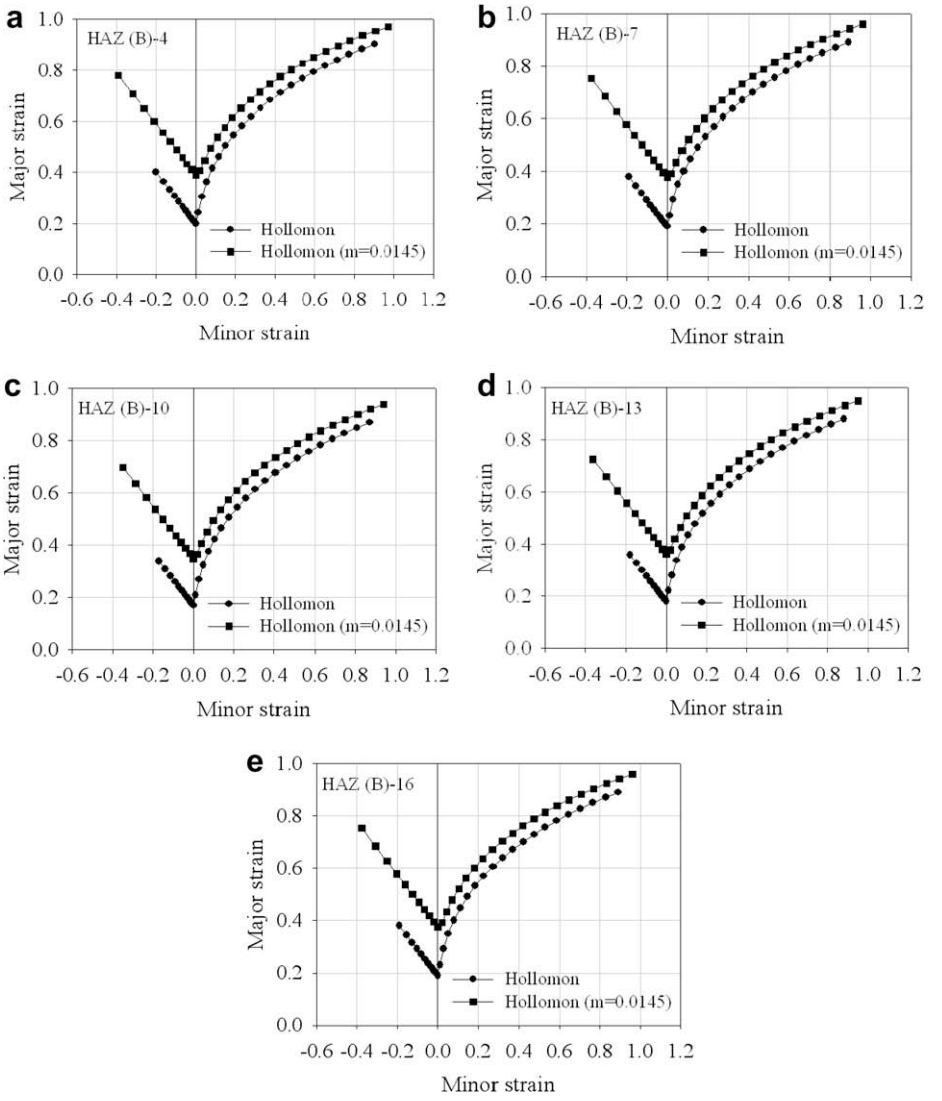

Fig. 14. Calculated forming limit diagrams for the HAZ(B): (a) HAZ(B)-4, (b) HAZ(B)-7, (c) HAZ(B)-10, (d) HAZ(B)-13 and (e) HAZ(B)-16 (the number # in HAZ # represents the distance from the weld zone center).

center of the weld zone, with the width of about 7 mm. The yield stress distributions at initial yielding and at $\bar{\varepsilon} = 0.2$ are illustrated in Fig. 10 for all locations of the welded DP590 sheet. The strength is the highest at the middle of the weld zone, while the lowest is at the boundaries between the weld zone and the HAZ (HAZ(A)-4, HAZ(B)-4, HAZ(C)-5) as shown in Figs. 9 and 10. Except for the boundaries having the lowest strength, the weld zones have a higher magnitude of strength than that of the base sheet.

In order to validate the proposed procedure, the procedure was applied for the base material for which the hardening curve is already available. As an input hardening data, the averaged hardening parameters (K = 1015.9 MPa, n = 0.232, $\bar{\varepsilon}_0 = 0.0262$) along the three directions shown in Table 4 were utilized for the indentation simulation and the resulting load–depth curve was compared with the experiment curve as shown in Fig. 11. The reasonably good agreement between the two curves confirms that the proposed procedure is reasonably reliable.

Besides utilizing the available hardening data, the hardening curve was also determined from the 840 combinations of the hardening parameters following the proposed procedure. The resulting hardening data (K = 980 MPa, n = 0.20, $\bar{\varepsilon}_0 = 0.013$), which is the same as those of HAZ(C)-24, was compared with that measured from the uni-axial tension test (for the rolling direction) in Fig. 12. The two curves agree well overall even though the particular parameters, especially n values, are different each other. This is because, when the Considere criterion is applied for the Swift hardening law, the uniform strains ($n - \bar{\varepsilon}_0$) are similar (with 0.187 and 0.209, respectively) and so are the initial yields stresses (with 411.2 and 433.4 MPa, respectively).

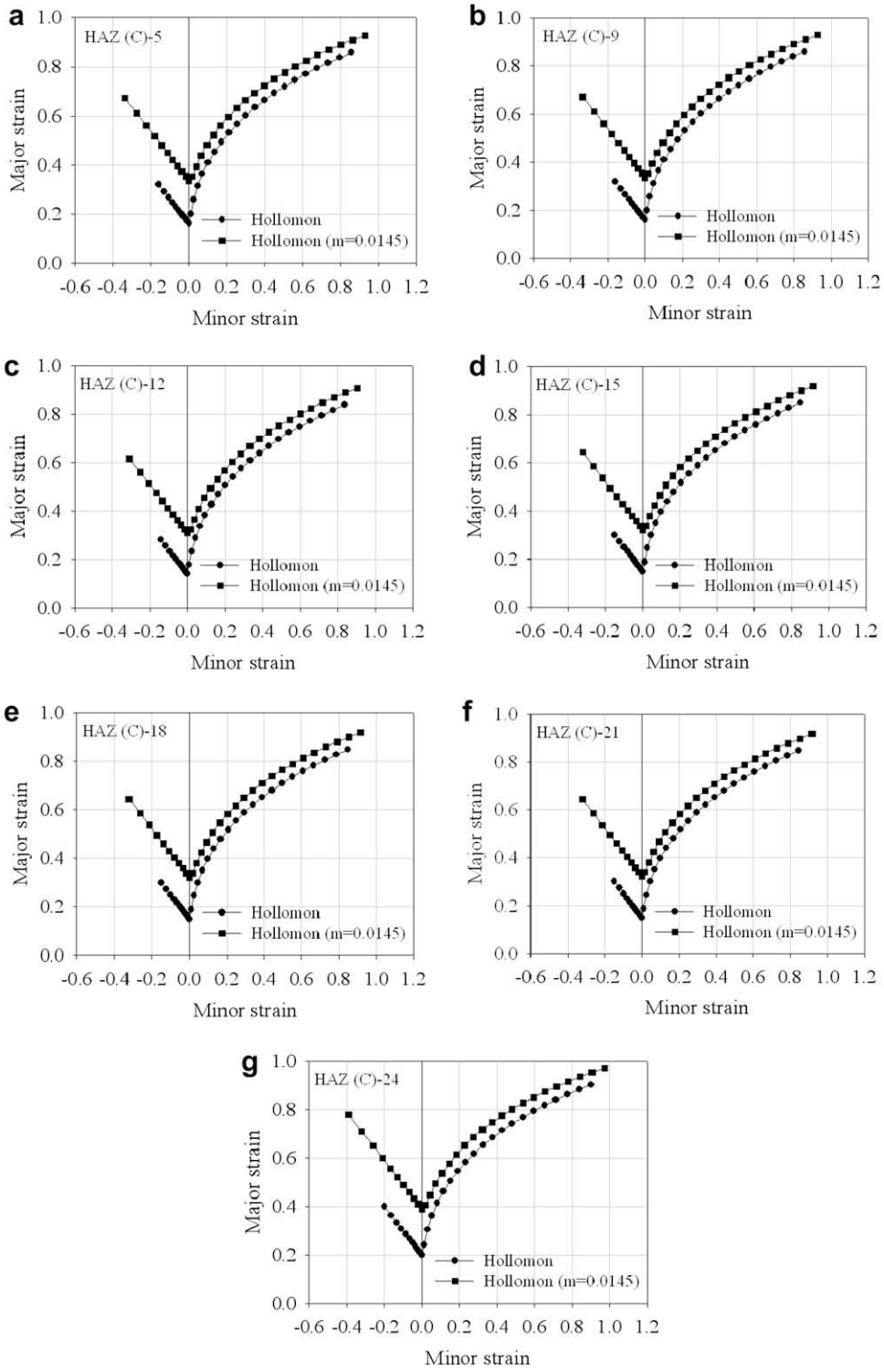

Fig. 15. Calculated forming limit diagrams for the HAZ(C): (a) HAZ(C)-5, (b) HAZ(C)-9, (c) HAZ(C)-12, (d) HAZ(C)-15, (e) HAZ(C)-18, (f) HAZ(C)-21 and (g) HAZ(C)-24 (the number # in HAZ # represents the distance from the weld zone center).

As for the plastic anisotropy, the weld zones were assumed to be isotropic. The yield function exponent and the strain-rate sensitivity index were assumed to be $M = 6.0$ and $m = 0.0145$, respectively, sharing the same values with the base material. The weld zones mostly consist of martensite and ferrite phases, which have BCT and BCC structures, respectively,

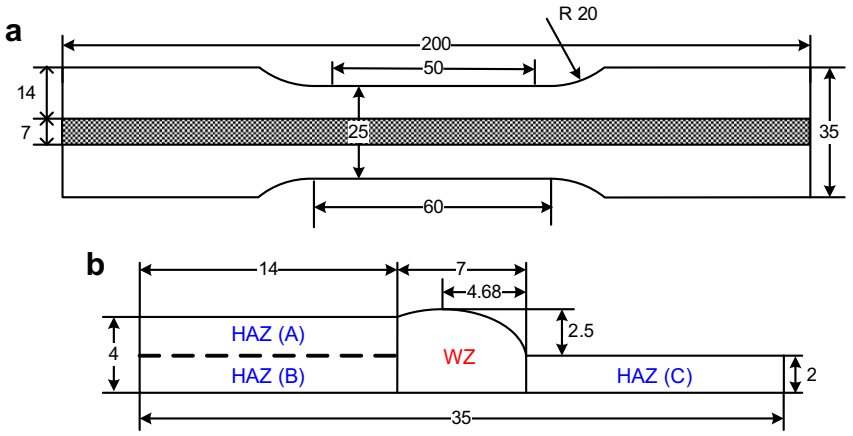

Fig. 16. Dimensions of the longitudinal welded specimen for uni-axial tension tests (in mm): (a) top view and (b) cross-section view (enlarged by five times in scale).

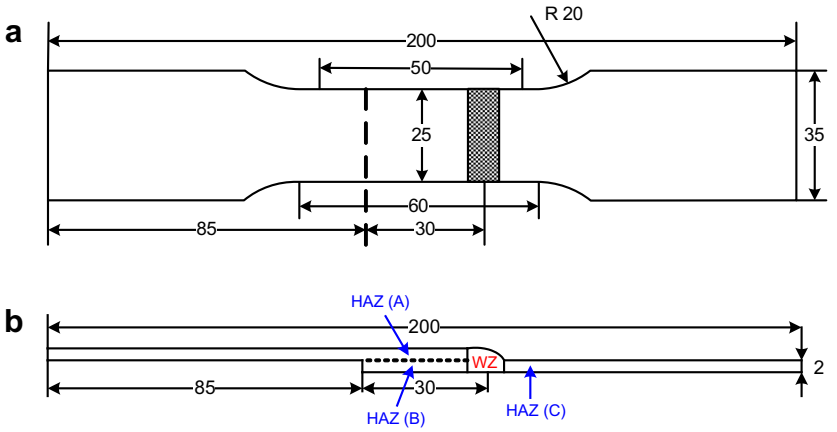

Fig. 17. Dimensions of the transverse welded specimen for uni-axial tension tests (in mm): (a) top view and (b) cross-section view.

therefore, the use of $M = 6.0$ is justified. As for the rate sensitivity, the thermal effect during the welding process was not considered here for simplicity.

The forming limit diagram was calculated at each location within the weld zones following the same procedure used for that of the base material and all results are shown in Figs. 13–15. The FLD calculations were conducted using the implemented Yld2000-2d with the isotropic condition and yield exponent, $M = 6$. Also, the initial defect parameter, $D_0 = 0.9997$, was commonly used for all cases in the calculation of the M–K theory. The forming limit values of the weld zones were slightly deteriorated compared to that of the base zone, particularly in the HAZ(C) zone.

Note that the forming limit diagrams are important for the formability performance of welded parts under various external loading conditions, particularly when the major principal stretching is aligned with weld lines. However, their importance significantly reduces if the major principal stretching is aligned vertically to the weld lines. In such a case, fracture is resulted by strain localization in which the size of the flow stress and thickness are much more important. These will be confirmed in the following verification based on the uni-axial tension test.

4. Verifications

Since the mechanical properties of the weld zones were indirectly measured utilizing the continuous indentation method and its FEM analysis, the uni-axial tension and three point bending tests were performed on the welded specimens to validate those properties. As previously mentioned, the 2D plane stress condition is imposed in this work for computational efficiency. Therefore, all numerical simulations were performed using the shell element.

4.1. Uni-axial tension tests

For the uni-axial tension test, the longitudinal and transverse welded specimens were prepared as illustrated in Figs. 16 and 17. Tension tests were conducted utilizing the standard specimen, KS B 0801 with Zwick's 10-t tension test machine at a

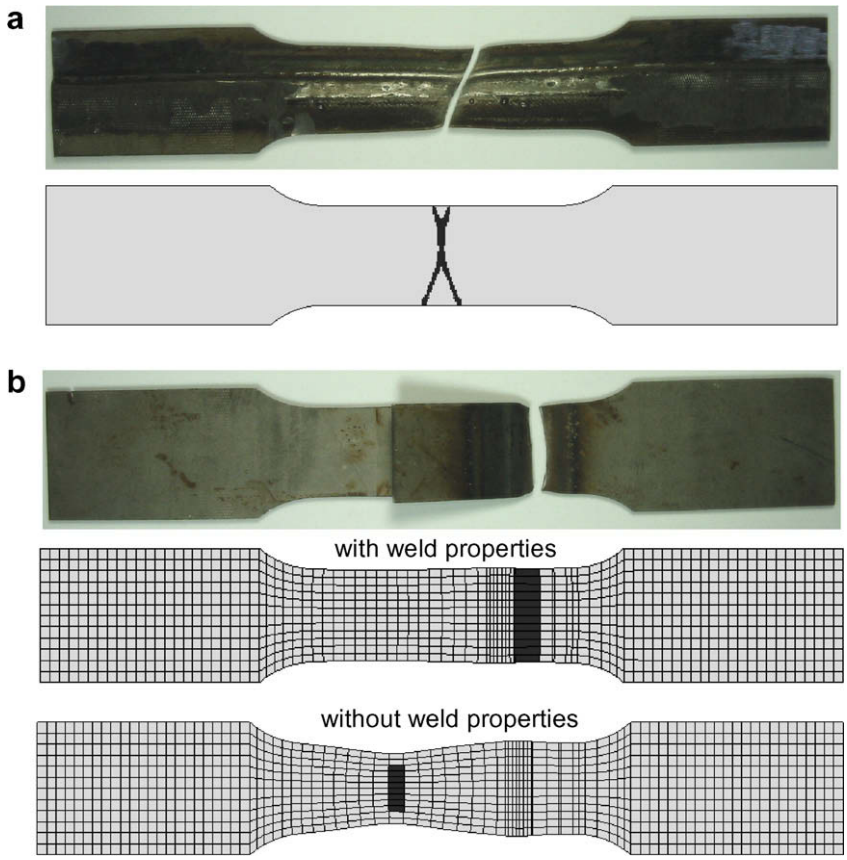

Fig. 18. Experimental and simulated results for uni-axial tension tests: (a) longitudinal specimen and (b) transverse specimen.

constant cross-head speed of 0.05 mm/s. The extension data was collected using Zwick's Macro-Standard extensometer with 50 mm gauge length. Note that tension tests for the longitudinal welded specimen were performed by inserting the base material (2.0 mm thickness) at the grip part because the cross-sectional thickness of the welded specimen was not uniform, as shown in Fig. 16.

Numerical simulations for the uni-axial tension tests were conducted utilizing the ABAQUS/Standard implicit code with the user subroutine UMAT. The reduced four node shell (S4R) elements with five integration points through thickness were used for all specimens. The element size of the specimen was approximately 2.0 mm $\times$ 2.0 mm with a finer mesh size of about 1.0 mm $\times$ 1.0 mm in the weld zones. For the longitudinal specimen, one shell plate was used, but with seven regions having different thicknesses to describe the thickness change at the weld zone shown in Fig. 16. For the transverse specimen, two shells having uniform thickness were used, which were joined together at the weld zone using TIE CONSTRAINT Option in the code. For the weld zones, the mechanical properties summarized in Table 5 and forming limit curves shown in Figs. 13–15 were assigned to each location based on the previously assumed stepwise homogeneous properties in the weld zones as illustrated in Fig. 6(b).

For the longitudinal specimen, failure initiated at HAZ(C)-12 in the center, because the specimen deformed under the iso-strain condition (for the longitudinal direction), while the forming limit curve of HAZ(C)-12 is the lowest among all materials. On the other hand, for the transverse specimen, it occurred at the boundary between the weld zone and the HAZ(C) because of the low strength at this location. In Fig. 18, the experimental failure locations show good agreement with the simulated results. Note here that, in order to simulate failure (or material split), all stress components were artificially assigned to be zero using the user subroutine developed in this work (to mimic the vanished resistance of failed elements) once elements reached FLD curves: material softening to account for material failure at FLD curves. Also note that the experimental failure line is slightly inclined for the longitudinal case in Fig. 18(a). This was successfully simulated using very fine meshes (0.4 mm $\times$ 0.4 mm). The simulated load-engineering strain profiles were also compared with the measured results in Fig. 19, which shows reasonably good agreement.

Note that the forming limit diagrams determine failure positions in load–displacement curves associated with the iso-strain condition for the longitudinal specimen; however, this is not the case for the transverse specimen because the strain localization associated with the force equilibrium condition determines failure (for which the stress and the thickness are far more important than FLD). For the experimental result of the longitudinal specimen, the yield point elongation is observed at

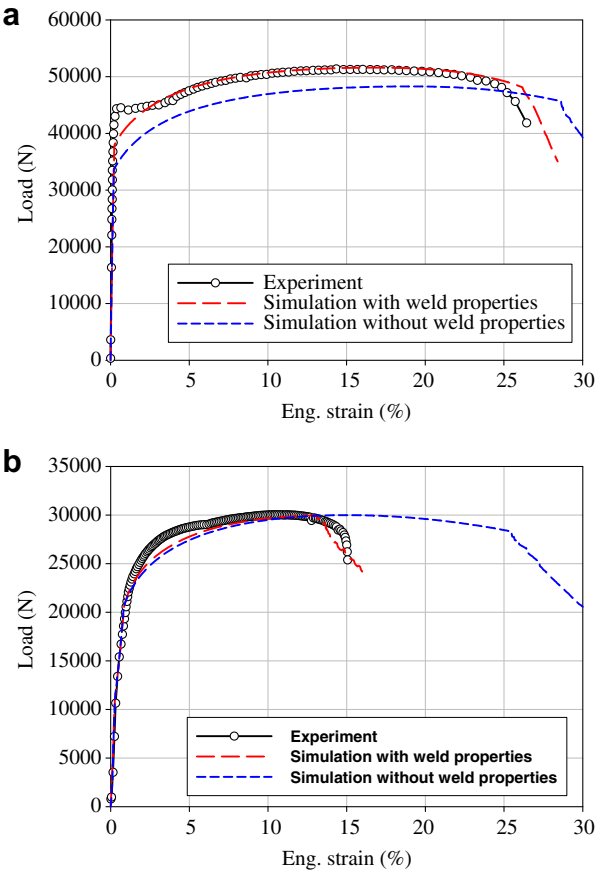

Fig. 19. Load vs. engineering strain profiles of uni-axial tension tests for the welded specimen: (a) longitudinal specimen and (b) transverse specimen.

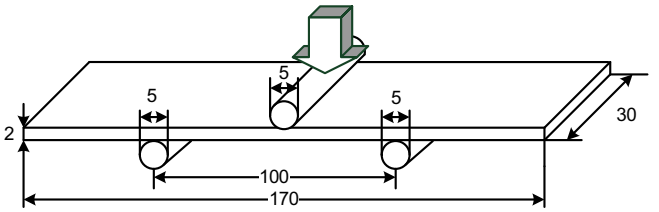

Fig. 20. The schematic diagram of the three point bending test (in mm).

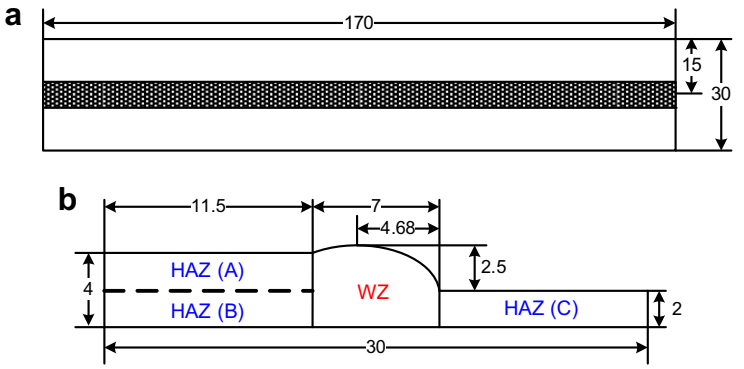

Fig. 21. Dimensions of the longitudinal welded specimen for three point bending tests (in mm): (a) top view and (b) cross-section view (enlarged by five times in scale).

the initial stage, which is the material characteristic of the annealed steel (Waterschoot et al., 2003). Since the yield point elongation was not observed for the base material here, it might be related to the weld properties, which was not observed in the indirect measurement.

4.2. Three point bending tests

To verify the indirectly measured weld zone properties, the three point bending tests were also performed using the welded specimens. Test dimensions are illustrated in Fig. 20 and tests were performed utilizing the MTS machine with 0.5-t capacity at a constant punch speed, 0.05 mm/s. The three point bending tests were also carried out for the longitudinal and the transverse specimens, whose top and cross-sectional views are shown in Figs. 21 and 22, respectively. In this test, the punch moved down, contacting the top of the weld zone for both specimens.

Finite element simulations were performed using ABAQUS/Standard with the user subroutine UMAT. The reduced four node shell (S4R) elements with five integration points through thickness were used for all specimens. The element size of the specimen was approximately 2.0 mm × 2.0 mm with a finer mesh size of about 1.0 mm × 1.0 mm in the weld zones and of about 0.2 mm × 1.0 mm in the contact regions. The friction coefficient was assumed to be 0.15, with which the simulation result of the three point bending test matched well with the experiment for the DP590 base sheet as shown in Fig. 23. Meshes were prepared in the same manner as done in the uni-axial tension tests, utilizing one shell plate for the longitudinal specimen and two shell plates tied together for the transverse specimen. Considering the symmetry, only the half of the specimen was simulated for the longitudinal case, while the whole was simulated for the transverse case. The mechanical properties of the weld zones were assigned to each location in the same manner as done in the uni-axial tension tests.

Figs. 24 and 25 show the bent shapes of specimens and the load–displacement curves of experimental and simulated results, respectively, which show good agreement for both the longitudinal and transverse tests, confirming that the indirectly measured weld zone properties are valid.

To understand the effects of the weld properties, simulations were also performed using base material properties for the whole weld zones (ignoring the weld properties). Those results are compared with those obtained considering the weld zone properties in Figs. 19 and 25. Fig. 19(b) demonstrates that using the weld properties is so important to properly predict the

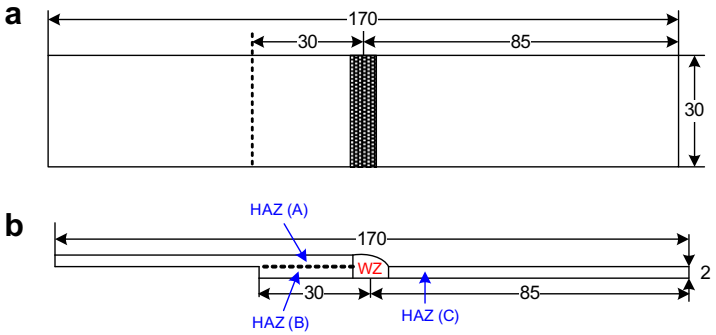

Fig. 22. Dimensions of the transverse welded specimen for three point bending tests (in mm): (a) top view and (b) cross-section view.

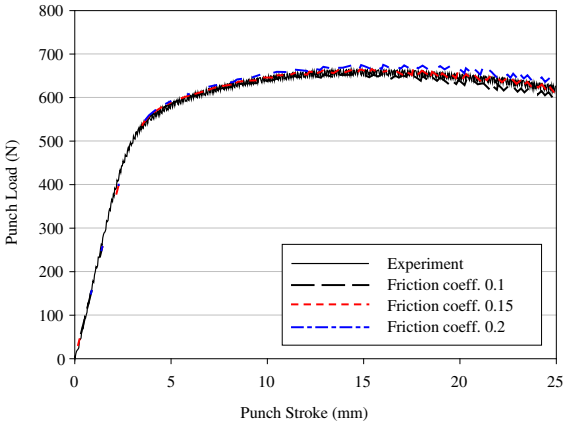

Fig. 23. Punch load vs. displacement profiles of three point bending tests for the DP590 base specimen with various friction coefficients.

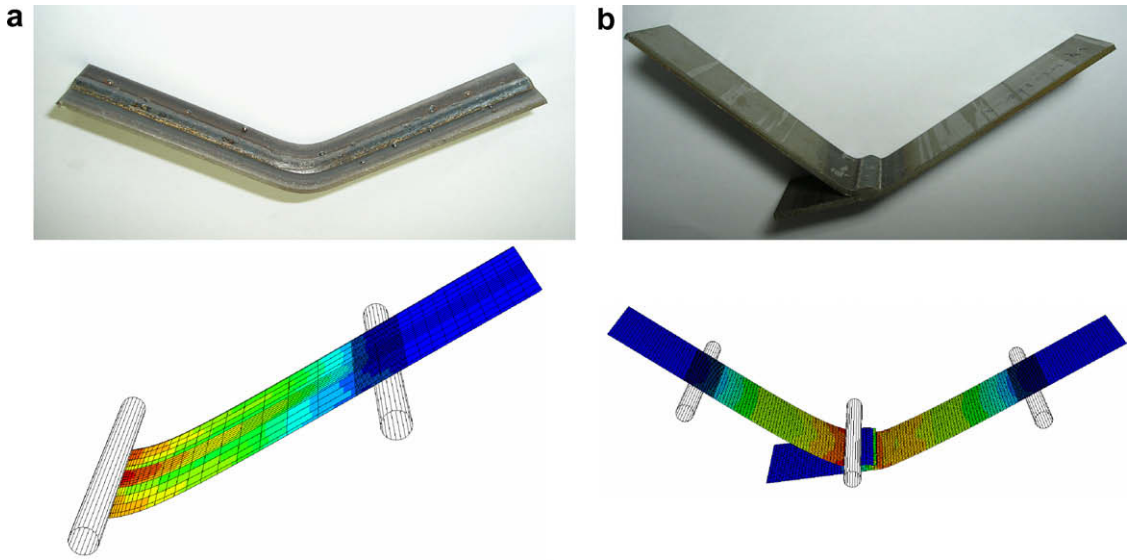

Fig. 24. Experimental and simulated results for three point bending tests: (a) longitudinal specimen and (b) transverse specimen.

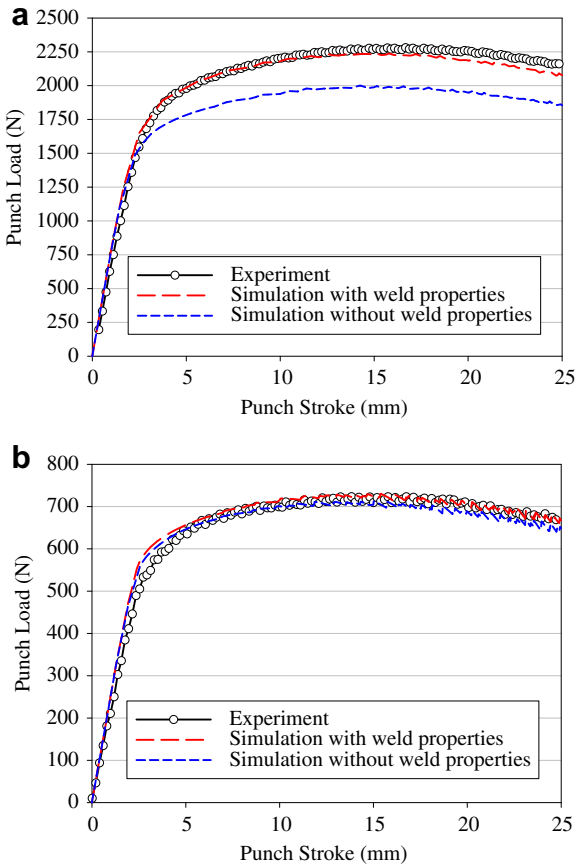

Fig. 25. Punch load vs. displacement profiles of three point bending tests for the welded specimen: (a) longitudinal specimen and (b) transverse specimen.

early failure in the transverse tension test, which is associated with the lowest strength at the boundary between the weld zone and HAZ, as confirmed also by Rodrigues et al. (2004a,b). Figs. 19(a) and 25(a) also demonstrates that the base material results significantly underestimate the loading level since higher strength at the weld zone is completely ignored, suggesting

the importance of utilizing the weld properties for the accurate performance evaluation in general. Note that the simulated results with and without weld properties, shown in Fig. 25(b), are almost the same because the strength of the area experiencing major deformation, which locates between HAZ(A)-4 and 7, is not so significantly different from that of the base sheet.

5. Summary

The welding process is an important joining technology in the automotive industry. As for the performance evaluation of welded automotive components associated with durability or crashworthiness, it is important to properly account for the property change near and in the weld zone, since the base material undergoes significant mechanical property changes when welded as a result of welding heat effects. Therefore, the method to characterize the mechanical properties of the metal active gas (MAG) weld zone and heat affected zone (HAZ) was developed utilizing the continuous indentation method along with its FEM analysis in this work. In order to verify the measured weld properties, experiments and simulations were performed for uni-axial tension and three point bending tests utilizing DP590 welded specimens. Experiments and simulations show good agreement, verifying the developed characterization method for the weld zones. Further comparison of the simulation results obtained with/without weld properties for uni-axial tension and three point bending tests also confirmed that the implementation of weld properties is important to improve the FEM prediction capability for the performance evaluation of the welded DP-steel automotive parts.

Acknowledgements

The authors would like to thank the Korea Science and Engineering Foundation (KOSEF) for sponsoring this research through the SRC/ERC program of MOST/KOSEF (R11-2005-065) and also appreciate the supports of GM and POSCO. Gratitude also goes to Drs. Lim Ji-Ho (POSCO) and Ro Dong-Seong (Frontics) for performing high strain-rate tests and indentation tests, respectively.

References

Abdullah, K., Wild, P.M., Jeswiet, J.J., Ghasempoor, A., 2001. Tensile testing for weld deformation properties in similar gage tailor welded blanks using the rule of mixtures. Journal of Materials Processing Technology 112 (1), 91–97.

Afrin, N., Chen, D.L., Cao, X., Jahazi, M., 2008. Microstructure and tensile properties of friction stir welded AZ31B magnesium alloy. Materials Science and Engineering A 472 (1–2), 179–186.

Ahn, J.-H., Kwon, D., 2001. Derivation of plastic stress–strain relationship from ball indentations: examination of strain definition and pileup effect. Journal of Materials Research 16 (11), 3170–3178.

Alcalá, J., Giannakopoulos, A.E., Suresh, S., 1998. Continuous measurements of load–penetration curves with spherical micro-indenters and the estimation of mechanical properties. Journal of Materials Research 13 (5), 1390–1400.

Antunes, J.M., Fernandes, J.V., Menezes, L.F., Chaparro, B.M., 2007. A new approach for reverse analyses in depth-sensing indentation using numerical simulation. Acta Materialia 55 (1), 69–81.

Aslanlar, S., Ogur, A., Ozsarac, U., Ilhan, E., Demir, Z., 2007. Effect of welding current on mechanical properties of galvanized chromided steel sheets in electrical resistance spot welding. Materials and Design 28 (1), 2–7.

Barlat, F., Lian, J., 1989. Plastic behavior and stretchability of sheet metals. Part. I. A yield function for orthotropic sheets under plane stress conditions. International Journal of Plasticity 5 (1), 51–66.

Barlat, F., Lege, D.J., Brem, J.C., 1991. A six-component yield function for anisotropic materials. International Journal of Plasticity 7 (7), 693–712.

Barlat, F., Becker, R.C., Hayashida, Y., Maeda, Y., Yanagawa, M., Chung, K., Brem, J.C., Lege, D.J., Matsui, K., Murtha, S.J., Hattori, S., 1997. Yielding description of solution strengthened aluminum alloys. International Journal of Plasticity 13 (4), 385–401.

Barlat, F., Brem, J.C., Yoon, J.W., Chung, K., Dick, R.E., Choi, S.-H., Pourboghrat, F., Chu, E., Lege, D.J., 2003. Plane stress yield function for aluminum alloy sheets-part 1: theory. International Journal of Plasticity 19 (9), 1297–1319.

Casals, O., Alcalá, J., 2005. The duality in mechanical property extractions from Vickers and Berkovich instrumented indentation experiments. Acta Materialia 53 (13), 3545–3561.

Chen, X., Drouin, J., Coopmans, D., Dell'Osso, R., Belanger, P., 2001. Stamping and crush performance of dual phase steel. SAE Technical Paper No. 2001-01-3074, SAE Publication, Warrendale, PA, 2001.

Chollacoop, N., Ramamurty, U., 2005. Experimental assessment of the representative strains in instrumented sharp indentation. Scripta Materialia 53 (2), 247–251.

Chollacoop, N., Dao, M., Suresh, S., 2003. Depth-sensing instrumented indentation with dual sharp indenters. Acta Materialia 51 (13), 3713–3729.

Chung, K., Richmond, O., 1993. A deformation theory of plasticity based on minimum work paths. International Journal of Plasticity 9 (8), 907–920.

Chung, K., Lee, M.-G., Kim, D., Kim, C., Wenner, M.L., Barlat, F., 2005. Spring-back evaluation of automotive sheets based on isotropic-kinematic hardening laws and non-quadratic anisotropic yield functions. Part I. theory and formulation. International Journal of Plasticity 21 (5), 861–882.

Dao, M., Chollacoop, N., Van Vliet, K.J., Venkatesh, T.A., Suresh, S., 2001. Computational modeling of the forward and reverse problems in instrumented sharp indentation. Acta Materialia 49 (19), 3899–3918.

Doerner, M.F., Nix, W.D., 1986. A method for interpreting the data from depth-sensing indentation instruments. Journal of Materials Research 1 (4), 601–609.

Dugdale, D.S., 1954. Cone indentation experiments. Journal of the Mechanics and Physics of Solids 2 (4), 265–277.

Fekete, J., Stibich, A., Shi, M., 2001. A comparison of the response of HSLA and dual phase sheet steel in dynamic crush. SAE Technical Paper No. 2001-01-3101, SAE Publication, Warrendale, PA, 2001.

Gery, D., Long, H., Maropoulos, P., 2005. Effects of welding speed, energy input and heat source distribution on temperature variations in butt joint welding. Journal of Materials Processing Technology 167 (2–3), 393–401.

Giannakopoulos, A.E., Suresh, S., 1997a. Indentation of solids with gradients in elastic properties. Part I. Point force. International Journal of Solids and Structure 34 (19), 2357–2392.

Giannakopoulos, A.E., Suresh, S., 1997b. Indentation of solids with gradients in elastic properties. Part II. Axisymmetric indentors. International Journal of Solids and Structure 34 (19), 2393–2428.

Giannakopoulos, A.E., Suresh, S., 1999. Determination of elastoplastic properties by instrumented sharp indentation. Scripta Materialia 40 (10), 1191–1198.

Hosford, W.F., 1972. A generalized isotropic yield criterion. Journal of Applied Mechanics 39 (2), 607–609.
Huh, H., Lim, J.H., Kim, S.B., Han, S.S., Park, S.H., 2004. Formability of the steel sheet at the intermediate strain rate. Key Engineering Materials, 403–408.
Jang, J., Choi, Y., Lee, Y.-H., Kwon, D., 2005a. Instrumented microindentation studies on long-term aged materials: work-hardening exponent and yield ratio as new degradation indicators. Materials Science and Engineering A 395 (1–2), 295–300.
Jang, K.C., Lee, D.G., Kuk, J.M., Kim, I.S., 2005b. Welding and environmental test condition effect in weldability and strength of Al alloy. Journal of Materials Processing Technology, 1038–1045.
Lee, M.-G., Kim, D., Kim, C., Wenner, M.L., Wagoner, R.H., Chung, K., 2005. Spring-back evaluation of automotive sheets based on isotropic-kinematic hardening laws and non-quadratic anisotropic yield functions. Part II. characterization of material properties. International Journal of Plasticity 21 (5), 883–914.
Liu, P., Li, Y., Geng, H., Wang, J., 2007. Microstructure characteristics in TIG welded joint of Mg/Al dissimilar materials. Materials Letters 61 (6), 1288–1291.
Logan, R.W., Hosford, W.F., 1980. Upper-bound anisotropic yield locus calculations assuming pencil glide. International Journal of Mechanical Sciences 22 (7), 419–430.
Marciniak, Z., Kuczynski, K., 1967. Limits strains in the processes of stretch-forming sheet metal. International Journal of Mechanical Sciences 9 (9), 609–620.
Marya, M., Gayden, X.Q., 2005. Development of requirements for resistance spot welding dual-phase (DP600) steels. Part I. The causes of interfacial fracture. Welding Journal 84, 172–182.
Millman, YU.V., Galanov, B.A., Chugunova, S.I., 1993. Plasticity characteristic obtained through hardness measurement. Acta Metallurgica et Materialia 41 (9), 2523–2532.
Nakamachi, E., Xie, C., Harimoto, M., 2001. Drawability assessment of BCC steel sheet by using elastic/crystalline viscoplastic finite element analyses. International Journal of Mechanical Sciences 43 (3), 631–652.
Oliver, W.C., Pharr, G.M., 1992. An improved technique for determining hardness and elastic-modulus using load and displacement sensing indentation experiments. Journal of Materials Research 7 (6), 1564–1583.
Paruz, H., Edmonds, D.V., 1989. The strain hardening behavior of dual-phase steel. Materials Science and Engineering A 117, 67–74.
Qiu, X.G., Chen, W.L., 2007. The study on numerical simulation of the laser tailor welded blanks stamping. Journal of Materials Processing Technology, 128–131.
Rodrigues, D.M., Menezes, L.F., Loureiro, A., 2004a. The influence of the HAZ softening on the mechanical behaviour of welded joints containing cracks in the weld metal. Engineering Fracture Mechanics 71 (13-14), 2053–2064.
Rodrigues, D.M., Menezes, L.F., Loureiro, A., Fernandes, J.V., 2004b. Numerical study of the plastic behaviour in tension of welds in high strength steel. International Journal of Plasticity 20 (1), 1–18.
Sato, Y., Sugiura, Y., Shoji, Y., Park, S.H., Kokawa, H., Ikeda, K., 2004. Post-weld formability of friction stir welded Al alloy 5052. Materials Science and Engineering A 369 (1–2), 138–143.
Saunders, F.I., Wagoner, R.H., 1996. Forming of tailor-welded blanks. Metallurgical and Materials Transactions A 27 (9), 2605–2616.
Suresh, S., Giannakopoulos, A.E., Alcalá, J., 1997. Spherical indentation of compositionally graded materials: theory and experiments. Acta Materialia 45 (4), 1307–1321.
Tabor, D., 1951. The Hardness of Metals. Clarendon Press, Oxford.
Thaulow, C., Paauw, A.J., Hauge, M., Toyoda, M., Minami, F., 1994. Fracture property of HAZ-notched weld joint with mechanical mis-matching. Part II. In: Schwalbe, K.-H., Koc¸ak, M. (Eds.), Mis-Matching of Welds, ESIS 17. Mechanical Engineering Publications, London, pp. 417–432.
Tirupataiah, Y., Sundararajan, G., 1991. A dynamic indentation technique for the characterization of the high-strain rate plastic-flow behavior of ductile metals and alloys. Journal of the Mechanics and Physics of Solids 39 (2), 243–271.
Venkatesh, T.A., Van Vliet, K.J., Giannakopoulos, A.E., Suresh, S., 2000. Determination of elasto-plastic properties by instrumented sharp indentation: guidelines for property extraction. Scripta Materialia 42 (9), 833–839.
Waterschoot, T., De, A.K., Vandeputte, S., De Cooman, B.C., 2003. Static strain aging phenomena in cold-rolled dual-phase steels. Metallurgical and Materials Transactions A 34 (3), 781–791.
Wojnowski, D., Oh, Y.K., Indacochea, J.E., 2000. Metallurgical assessment of the softened HAZ region during multipass welding. Journal of Manufacturing Science and Engineering 122 (2), 310–315.
Woo, W., Choo, H., Brown, D.W., Liaw, P.K., Feng, Z., 2006. Texture variation and its influence on the tensile behavior of a friction-stir proceeded magnesium alloy. Scripta Materialia 54 (11), 1859–1864.
Zeng, K., Soderlund, E., Giannakopoulos, A.E., Rowcliffe, D.J., 1996. Controlled indentation: a general approach to determine mechanical properties of brittle materials. Acta Materialia (44), 1127–1141.